

Carbon Nanotubes versus Graphene as Flexible Transparent Electrodes in Inverted Perovskite Solar Cells

Il Jeon,^{†+} Jungjin Yoon,^{‡+} Namyoung Ahn,[‡] Mohamed Atwa,[†] Clement Delacou,[†] Anton Anisimov,[#] Esko I. Kauppinen,[§] Mansoo Choi,^{‡} Shigeo Maruyama,^{†,&*} and Yutaka Matsuo^{†,£*}*

[†]: Department of Mechanical Engineering, School of Engineering, The University of Tokyo, Tokyo 113-8656, Japan

[‡]: Department of Mechanical and Aerospace Engineering, Seoul National University, Seoul 08826, South Korea

[#]: Canatu Ltd., Konalankuja 5, FI-00390 Helsinki, Finland

[§]: Department of Applied Physics, Aalto University School of Science, FI-00076 Aalto, Finland

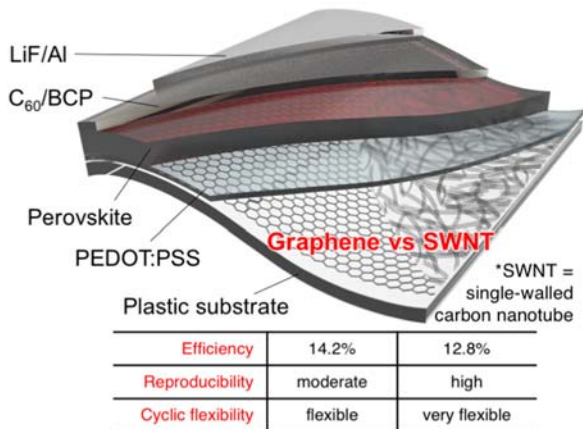
[&]: National Institute of Advanced Industrial Science and Technology (AIST), Ibaraki 305-8564, Japan

[£]: Hefei National Laboratory for Physical Sciences at Microscale, University of Science and Technology of China, Anhui 230026, China

Abstract

Transparent carbon electrodes composed of single-walled carbon nanotubes or graphene were used as the bottom electrode in flexible inverted perovskite solar cells. Their photovoltaic performance and mechanical resilience were compared and analyzed using various techniques. Whereas a conventional inverted perovskite solar cells using indium tin oxide showed a power conversion efficiency of 17.8%, the carbon nanotube- and graphene-based cells showed efficiencies of 12.8% and 14.2%, respectively. A thin layer of MoO₃ was used for its stable doping effect. The difference in photovoltaic performance between the carbon nanotube- and graphene-based cells was due to the inferior morphology and lower transmittance of the carbon nanotube films compared with the graphene films. Raman spectroscopy and four-probe measurements after strain application revealed that the graphene-based cells were more susceptible to strain than the carbon nanotube-based cells for a given magnitude of strain. Cyclic flexural testing also showed higher resilience of the carbon nanotube-based cells compared with graphene-based cells, though the difference was marginal. Overall, graphene is a better option than carbon nanotubes as the bottom transparent electrode in perovskite solar cells. However, the transfer step for graphene has lower reproducibility, and thus the development of better graphene transfer methods would help maximize the current capacity of graphene-based cells.

TOC



KEYWORDS: Carbon nanotubes, Graphene, Perovskite solar cells, Flexible solar cells, Carbon electrodes

Organohalide lead perovskite solar cells (PSCs) have progressed remarkably over the past seven years, with improvements being achieved in terms of both power conversion efficiency (PCE) and flexibility.¹⁻⁶ Several groups around the world have reported PCEs exceeding 20% in PSCs.^{7,8} To realize the full potential of PSCs, it is necessary to replace the indium tin oxide (ITO) electrode commonly used in PSCs. ITO has numerous limitations including the scarcity of indium, inflexibility,⁹ and degradation from exposure to poly(ethylenedioxythiophene):poly(styrene sulfonate) (PEDOT:PSS).¹⁰ Carbon nanotubes (CNTs) and graphene are potentially viable alternatives for PSC electrode materials considering the abundance of their elemental constituent carbon, their mechanical resilience, and their high performance in PSCs.^{11,12}

Since Iijima first reported CNTs,¹³ concentric CNTs have shown promise for use as electrodes in electronics.¹⁴⁻¹⁶ CNTs have high electrical conductivity and optical transparency,

resulting from their network of essentially infinitely conjugated double bonds.^{17,18} Recently, Kauppinen and colleagues have reported aerosol-synthesized single-walled carbon nanotube (SWNT) films that have high electrical conductivity and transparency, and can be applied to any substrate by direct, dry transfer.^{19–24}

Graphene, the other proposed PSC electrode material in this work, was only a hypothetical material until it was discovered by a research group in Manchester, England, in 2004.²⁴ Single-atom thick graphene is more conductive and transparent than CNTs. Graphene films are usually prepared by wet transfer and also have outstanding performance when used in place of conventional electrodes in photovoltaic applications.^{9,26–31}

In this work, we fabricated flexible, indium-free inverted PSCs by replacing ITO with SWNTs¹¹ or graphene¹². Then, we compared their feasibility as flexible transparent electrodes considering both photovoltaic and mechanical properties. To our knowledge, no such direct, detailed comparison between CNT and graphene films as PSC electrode materials has been reported.

For this study, we used stable MoO_x for doping.³² This is because the most established and chemically stable dopant should be used for the sake of valid comparison between the carbon electrodes. Unlike ionic dopants, such as HNO_3 , a transition metal dopant MoO_3 is reported to be one of the most stable and widely used for both SWNT and graphene electrodes.^{33–35} The morphology and transparency of graphene are better than those of SWNTs, and thus graphene produces higher PCE when used as the transparent electrode in inverted PSCs. However, SWNT-based PSCs have slightly better mechanical properties than those of graphene-based PSCs. This may be attributable to the randomly oriented entanglement of SWNTs and their defect-free nature, in contrast with strained graphene film, which have grain boundaries and defects.

An inverted architecture of PSCs was used for this study.³⁶ This is because such structures do not require high-temperature processing, enabling use in flexible electronics, which have plastic substrates that would melt under high temperatures. CNTs and monolayer graphene as the bottom electrode have previously been used to replace ITO in such inverted structures.^{11,30,37}

We began by fabricating reference PSCs using ITO glass substrates via the adduct method³⁸ and achieved a PCE of 17.7% (Figure 1a and b, Table 1). It has been argued that MoO₃ is not compatible with either SWNT¹² or CH₃NH₃PbI₃ (MAPbI₃)²⁹, but Sung *et al.*³⁰ discovered that depositing an ultrathin layer of MoO₃ (approximately 2 nm) can impart both doping and hole-transporting functionality to the PSCs without disturbing the alignment of the energy levels. To test this with SWNTs, we employed 2- and 6-nm-thick MoO₃ layers and fabricated SWNT-based PSCs without thermal treatment. The 2-nm-thick MoO₃-deposited SWNT PSCs had a higher PCE of 12.8% compared with the PCE of 11.0% for the 6-nm-thick MoO₃-deposited SWNT PSCs (Figure 1c and d, Figure S1a, Table 1). From the photovoltaic parameters, we can see that using a thicker MoO₃ layer decreased both the fill factor (FF) and the short-circuit current density (J_{SC}). We conjecture that these parameters decreased due to energy misalignment when the thicker layer was used. The higher series resistance (R_s) in the 6-nm-thick MoO₃-deposited PSCs is consistent with this, while the increase in shunt resistance (R_{SH}) is suspected to result from the increased hole-transporting ability of the thicker MoO₃ layer. The photoelectron yield spectra showed that the Fermi level increased with MoO₃ deposition thickness (Figure S2). The 6-nm-thick MoO₃ layer increases the Fermi level above that of PEDOT:PSS (5.1 eV), which is energetically unfavorable. MoO₃ with thickness below 6 nm is optimal for band-matching in PSCs.

We also fabricated graphene-based PSCs using wet-transferred graphene followed by deposition of a 2-nm-thick MoO₃ layer (Figure 1e, Figure S1b). A PCE of 14.2% was obtained,

which is higher than that of SWNT-based PSCs (Figure 1f, Table 1). This high efficiency arose mainly from a higher J_{SC} and higher open-circuit voltage (V_{OC}). The higher J_{SC} is attributed to the intrinsically high transmittance of single-layered graphene in contrast with that of the intertwined SWNTs (Figure S3). In fact, the graphene film showed a higher transmittance than that of even ITO. The difference in V_{OC} can be ascribed to the difference in surface morphology between the two carbon electrodes, which arises from the geometry of the materials.

Shunt pathways between the photoactive layer and the electrode decrease V_{OC} .⁴⁰ To investigate this in detail, we fabricated SWNT-based PSCs that are strong but not very durable by using HNO_3 dopant instead of MoO_3 (Figure 1g, Figure S1c). The HNO_3 -doped SWNT-based PSCs showed PCE of 15.3%, which is significantly higher than that of the MoO_3 -doped PSCs (Figure 1h, Table 1). The exceptionally strong doping of HNO_3 led to a high FF as indicated by four-probe sheet resistance measurement (Table S1), despite the high Fermi level (Figure S2f). J_{SC} in these was still lower than that of the graphene-based PSCs because of the intrinsically low transparency of the SWNT film (Figure S3) and possibly because of energy mismatch. However, these PSCs did exhibit higher V_{OC} than the 6-nm-thick MoO_3 -deposited SWNT-based PSCs. This supports our hypothesis that thick MoO_3 -deposited SWNTs have problems with shunt pathways resulting from poor morphology.

Table 1. Photovoltaic parameters of PSCs fabricated in this work under AM 1.5G simulated sunlight of 1 sun (100 mW cm⁻²). Average values can be found in Table S2.

Substrate	Anode	V _{oc} (V)	J _{sc} (mA cm ⁻²)	FF	R _s (Ω cm ²)	R _{sh} (Ω cm ²)	PCE
glass	ITO/PEDOT:PSS	0.99	21.6	0.83	27.0	73000	17.8%
	SWNT/MoO ₃ (2nm)/PEDOT:PSS	0.96	17.5	0.76	76.1	1500	12.8%
	SWNT/MoO ₃ (6nm)/PEDOT:PSS	0.90	16.9	0.71	114	2500	11.0%
	graphene/ MoO ₃ (2nm)/PEDOT:PSS	0.96	21.2	0.70	84.6	8100	14.2%
	SWNT-HNO ₃ /PEDOT:PSS	0.98	19.9	0.78	44.0	3000	15.3%
PEN	ITO/PEDOT:PSS	0.96	20.1	0.83	30.7	35000	16.0%
	SWNT/MoO ₃ (2nm)/PEDOT:PSS	0.90	18.8	0.65	151	1500	11.0%
	graphene/MoO ₃ /PEDOT:PSS	0.97	20.0	0.69	115	6200	13.3%

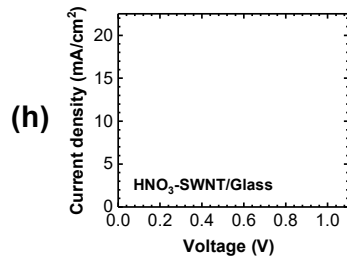
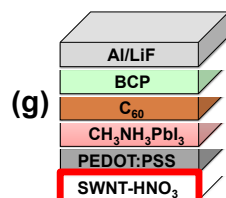
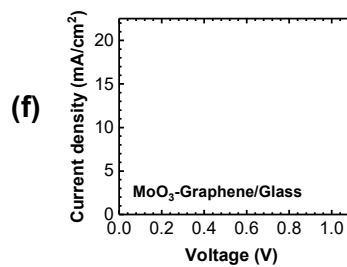
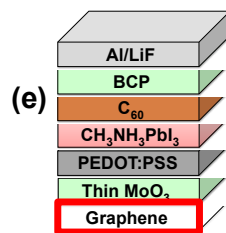
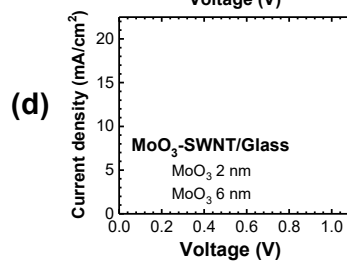
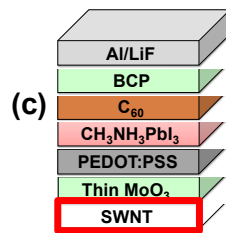
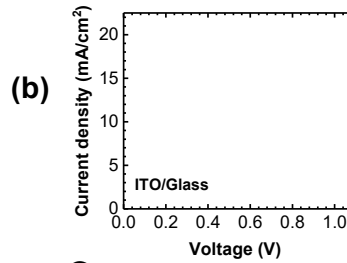
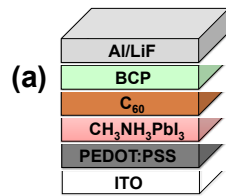


Figure 1. PSC structures and corresponding current density–voltage (J – V) curves of (a)(b) ITO reference PSCs, (c)(d) SWNT-based PSCs with MoO₃, (e)(f) graphene-based PSCs, and (g)(h) SWNT-based PSCs with HNO₃ doping.

Cross-sectional scanning electron microscopy (SEM) images of the devices (Figure S1) showed that the SWNT films have a rougher surface than the graphene or ITO films. The top SEM images in Figure S4, although not clear, also indicate that the SWNT films are much rougher than the graphene films. Atomic force microscopy (AFM) images corroborate these observations, showing that the SWNT films had a much higher average roughness value ($R_a = 15.1$ nm) as compared with the graphene films ($R_a = 3.5$ nm) (Figure 2). It is interesting to note that R_a of the SWNT films increased with increasing MoO₃ layer thickness, whereas that of the graphene films decreased after MoO₃ deposition. This is because thermal deposition or sputtering methods result in an even rougher surface when the target substrate for deposition is initially rough.⁴¹ Although a PEDOT:PSS overcoating was applied to smooth its surface, the SWNT/MoO₃ (6 nm)/PEDOT:PSS film still exhibited an R_a of 16.4 nm following the application of the PEDOT:PSS coating. HNO₃-SWNT/PEDOT:PSS, on the other hand, had R_a of 7.6, which was not rough enough to undermine V_{oc} . Graphene films, owing to their intrinsically flat surface, showed a maximum R_a of 5.6 nm. Therefore, we conclude that graphene outperforms SWNTs when used as the bottom electrode together with MoO₃ in PSCs, owing to the better morphology and higher transmittance of graphene compared with SWNT films. Regardless of other variations, none of the carbon electrode-based devices showed hysteresis (Figure S5). For SWNT films to perform as well as graphene as the bottom electrode in PSCs, it is necessary to minimize roughness and to avoid a film deposition on top of it.

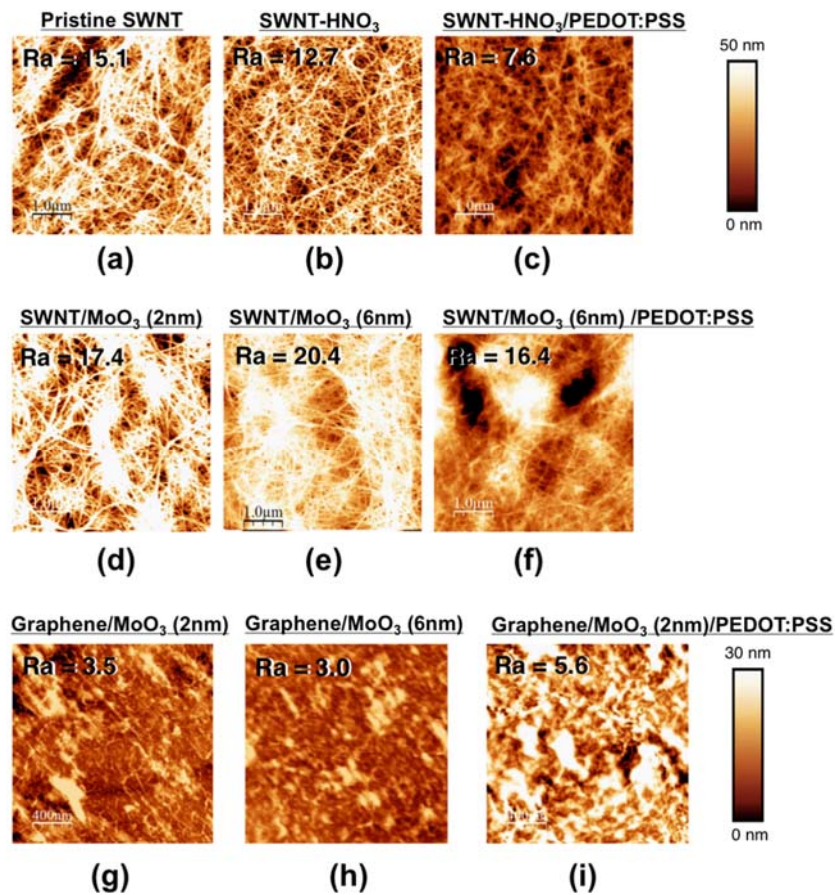


Figure 2. AFM images of (a) pristine SWNT film, (b) HNO₃-doped SWNT film, (c) HNO₃-doped SWNT film with a PEDOT:PSS overcoat, (d) 2-nm-thick MoO₃-deposited SWNT film, (e) 6-nm-thick MoO₃-deposited SWNT film, (f) 6-nm-thick MoO₃-deposited SWNT film with a PEDOT:PSS overcoat, (g) pristine graphene, (h) 2-nm-thick MoO₃-deposited graphene, and (i) a 2-nm-thick MoO₃-deposited graphene with a PEDOT:PSS overcoat.

Statistical analysis (Table S2) showed that all of the carbon electrode-based PSCs had highly reproducible performance. It is worth noting that SWNT-based devices have slightly higher performance variability, which we attribute to the rough surface of the SWNT films. However, these data were collected for only PSCs fabricated on high-quality carbon electrodes and PSCs for which electrode transfer failed were excluded. The transfer success rate was 4 out of 5 for SWNT films but only 3 out of 10 for graphene films. This is because the SWNT films that we used were dry-transferrable and did not have the problems of crumpling, thanks to their entangled geometry. Single-layered graphene, on the other hand, was easily broken or crumpled during wet transfer. Thus, the SWNT-based devices exhibited higher reproducibility than the graphene-based devices when the transfer process is also taken into account.

We studied the effect of mechanically straining the carbon electrodes by taking four-probe measurements and Raman spectra before and after the carbon electrodes were stretched and bent. We used polydimethylsiloxane (PDMS) as the substrate for this study because it has high elasticity, and more importantly, because its Raman peaks do not overlap with those of the carbon electrodes.⁴²

Both SWNT films and graphene films have extremely high elasticity.⁴³ However, stretching or bending can alter their electronic structure. This is of particular importance, because a change in electronic structure could undermine the electrical properties of the PSC.⁴⁴⁻⁴⁶ We suspected that graphene, which has grain boundaries, would have higher strain than SWNTs under bending and stretching because grain boundaries experience stronger strain when strain is homogeneously distributed along the graphene grains.⁴⁷⁻⁴⁹ We used a four-probe measurement to study the change in sheet resistance (R_{sheet}) of the carbon electrodes in a 100-cycle flexural test.

The results show that R_{Sheet} of the graphene film increased, whereas that of SWNT films stayed the same (Table S2). We attribute this to defect formation at the grain boundaries of graphene, which are absent from SWNT films.

We also conducted Raman mapping of the SWNT and graphene films to visualize the boundary defects that form when the film is stretched. The D band originates from a single in-plane transverse optical (iTO) phonon combined with phonon scattering from a defect, and it offers information about the strain at grain boundaries.^{42,50–52} The G band (E_{2g} mode at the Γ -point) originates from a first-order single-phonon Raman process, and it is affected by strain both within grains and at grain boundaries. Therefore, by observing D/G ratio across the surface of the films before and after stretching, we can identify damage to the grain boundaries. The damaged grain boundaries exhibit vibrations that are otherwise forbidden in a perfectly hexagonal carbon lattice, thus dramatically increasing the D/G ratio.⁵³ However, according to our measurement (Figure S6), there was no notable difference in the Raman mapping images of SWNT and graphene before and after stretching. This can be attributed to the boundary defects of graphene being too small in size to be discernible in the D/G ratio and to practical limitations in the measurement of such defect manifestation under strain.

We looked at the shifts of the G and 2D band peaks of the carbon electrodes under stretching and bending. The shift of these peaks with strain is an intrinsic property of hexagonal carbon rings and is defined by the Grüneisen parameters, which describe how changing the volume of a crystal lattice affects the vibrational Raman frequency of the phonons within the lattice.⁵⁴ The second-order two-phonon process responsible for the 2D band is caused by the scattering of two iTO phonons near the K point. This mode is independent of defects, but dependent on strain.⁵⁵ From Figure 3a-d, we can see that there are stronger shifts of the G and 2D bands in graphene

films than in SWNT films when the films are stretched and bent. This indicates that graphene is more susceptible to strain than SWNTs when the same magnitude of tensile or flexural force is applied. This is reasonable because the SWNT films, which are an entangled network of nanotubes, require more stretching for the hexagonal carbon rings in SWNTs to accumulate as much strain as those of graphene, which are immediately warped from in their original shape when stretched. Such difference potentially leads to the mechanical resilience of SWNTs electrodes compared with graphene electrodes.

Flexible PSCs were fabricated using SWNTs and graphene on polyethylene naphthalate (PEN) substrates (Figure 3e). Application of HNO_3 caused the carbon electrodes to turn yellow, which we suspect was due to the reaction between HNO_3 and the metal contact (Figure S7). Therefore, HNO_3 doping was not carried out during flexible PSC fabrication. From the photovoltaic results in Table 1, we can see that carbon electrode-based flexible devices with a 2-nm- MoO_3 layer showed similar PCEs to those of glass-based devices. SWNT-based flexible PSCs had a PCE of 11.0%, while graphene-based flexible PSCs had a PCE of 13.3%. Again, the photovoltaic performance of the unstrained graphene PSCs was better than of the unstrained SWNTs PSCs. However, this was reversed after the cyclic flexural test, with the SWNT PSCs exhibiting higher PCEs than the graphene PSCs. While all carbon electrode-based flexible PSCs exhibited higher mechanical robustness, the SWNT-based flexible PSCs were slightly more resilient than the graphene-based flexible PSCs (Figure 3f). This is consistent with our mechanical investigations of the carbon electrodes, which indicated that SWNTs had fewer defects and a lower susceptibility to strain-induced decreases in performance as compared with graphene. Nevertheless, this difference was smaller than we anticipated, which we speculate was due to the high elasticity of both carbon electrodes. Although stretching and bending may induce defects around the grain

boundary while strain is being applied, the electrical properties recover when the strain is removed.^{52,56,57} It has been reported that the perovskite active layer can also be damaged after 5000 cycles of severe bending test as the grain boundaries of polycrystalline perovskite may induce pinholes.⁵⁸ However, the degree of the damage is negligible compared with the degradation induced by the transparent electrode.

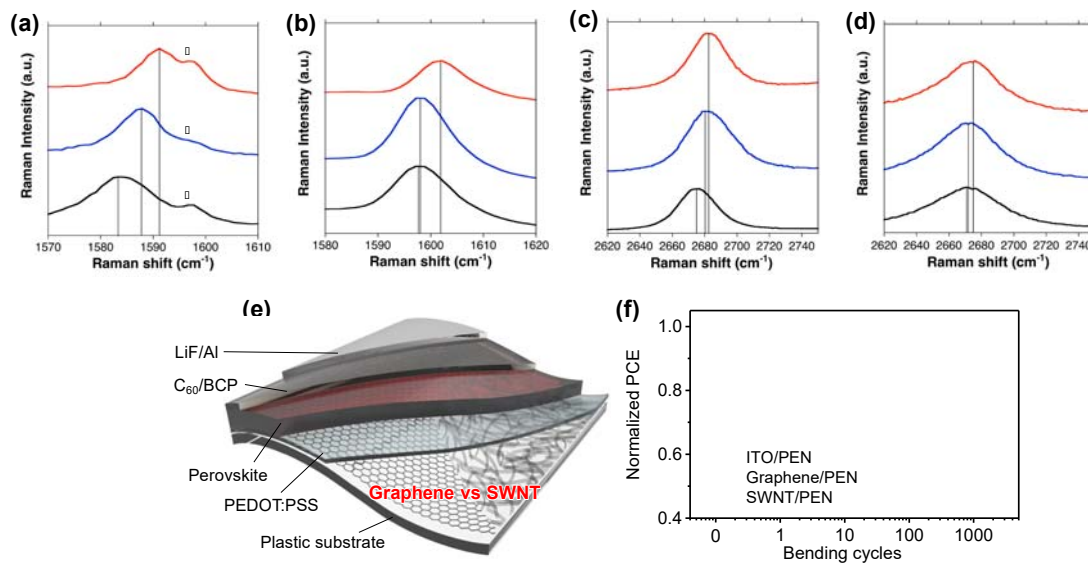


Figure 3. Raman spectra: (a) G band of graphene (black) when strained to 0.2% elongation (blue) and when bent in half (red), (b) D band of graphene (black) when strained to 0.2% elongation (blue) and when bent in half (red), (c) G band of the SWNT film (black) when strained to 0.2% elongation (blue) and when bent in half (red), and (d) D band of the SWNT film (black) when strained to 0.2% (blue) elongation and when bent in half (red). The peaks with a star in (a) indicate the peaks from the PDMS substrate. (e) Schematic illustration of the flexible PSCs using graphene and SWNT on a PEN substrate. (f) Cyclic flexural test results for flexible PSCs using ITO/PEN (black), graphene/PEN (green), and SWNT/PEN (red).

In conclusion, we compared the feasibility of two widely used transparent carbon electrode materials, namely, SWNT and graphene, as the bottom electrode in inverted PSCs. The photovoltaic performance of the graphene-based PSCs was higher than that of the SWNT-based PSCs owing to their better morphology as shown by AFM and their higher transparency as evidenced by UV-Vis spectroscopy. All the carbon electrode-based PSCs showed high reproducibility with no hysteresis, although the success rate of electrode transfer was much lower

for graphene than for SWNT films. The SWNT-based flexible PSCs showed marginally higher mechanical stability than the graphene-based flexible PSCs, due to the entangled configuration of the nanotube network and their inherent defect-free nature. We conclude that graphene is a better choice than SWNT for use as the bottom transparent electrode in PSCs. Flatter, more transparent SWNT films could hypothetically lead to even greater PSC performance, possibly outperforming graphene. However, for the graphene electrode, a more consistent and facile graphene transfer method is needed to improve the reproducibility and, thus, CNT electrodes is better for commercialization as an electrode for PSCs.

EXPERIMENTAL METHODS

Synthesis of SWNT Films. SWNTs were synthesized by an aerosol (floating catalyst) CVD method based on ferrocene vapor decomposition in a CO atmosphere. The catalyst precursor was vaporized by passing ambient temperature CO through a cartridge filled with ferrocene powder. The flow containing ferrocene vapor was then introduced into the high-temperature zone of a ceramic tube reactor through a water-cooled probe and mixed with additional CO. To obtain stable growth of SWNTs, a controlled amount of CO₂ was mixed with the CO carbon source. SWNTs were directly collected downstream of the reactor by filtering the flow through a nitrocellulose or silver membrane filter (Millipore Corp., USA; HAWP, 0.45 μm pore diameter).

Synthesis of Graphene Films. Continuous films of graphene were synthesized by means of alcohol-catalytic chemical vapor deposition (ACCVD) on copper using ethanol as the carbon source. Commercial copper foil (Nilaco Corp., CU-113303) was successively sonicated in HCl, DI-water, and IPA for 10 minutes each. The cleaned foil was then left to oxidize on a hot plate at 250°C for 1 hour. After oxidation, the foil was crimped in the shape of a pocket enclosure and loaded into the quartz tube of a home-made CVD reaction chamber that was evacuated to 15 Pa. The reaction chamber was heated to the target temperature of 1065°C under a constant flow rate of 300 sccm of 3% H₂ diluted in Argon throughout the reaction. A butterfly valve was used to maintain the total pressure within the quartz tube at 300 Pa for the duration of the growth procedure. After reaching the target temperature of 1065°C, the copper foil was left to anneal for one additional hour under constant flow of Ar/H₂. After the annealing process was completed, a constant flow of 0.1 sccm of

ethanol vapor was introduced to initiate growth. Growth times (as measured from start of the introduction of the ethanol vapor) varied between 4 and 10 hours, with longer growth times leading to larger graphene single crystals. It took 8-10 hours of growth to yield fused regions of graphene single crystals, leading to a continuous, conductive film of graphene. Upon completion of the growth step, the furnace was turned off and the quartz tube bearing the graphene-impregnated copper films was cooled using a fan for 30 minutes under the flow of 300 sccm Ar gas to prevent the collapse of the copper pockets. Immediately after synthesis and cooling, the pocket was opened and subjected to a contrasting oxidation on a hotplate at 250°C for 1 minute to discern the regions of the copper films with graphene (which did not oxidize) from those without graphene, which developed a colorful film of copper oxide. The regions bearing continuous graphene film were then transferring using the wet-etching poly(methyl methacrylate) (PMMA) transfer process explained extensively in previous works.

Solar Cell Fabrication. The ITO devices were fabricated on a commercially obtained ITO-coated glass substrates (AMG, $9.5 \Omega \text{ cm}^{-2}$, $25 \times 25 \text{ mm}^2$). The ITO-coated glass substrates were used after sequential cleaning in acetone, isopropanol, and deionized water using an ultrasonic bath (15 min each), followed by drying with nitrogen gas and storing in an oven at 120 °C. Right before use, the ITO-coated glass substrates were subjected to UV-O₃ treatment for 30 min.

The ultrathin MoO₃ layer was deposited on graphene-, SWNT-, ITO-coated glass substrates – except HNO₃-treated SWNT substrates – at a deposition rate of 0.1 \AA s^{-1} using a vacuum thermal evaporator, followed by an anaerobic annealing at 200 °C for 30 min. The deposition rate and the thickness were monitored by a quartz crystal sensor during the deposition. To prepare highly uniform PEDOT:PSS (Clevios P VP Al 4083), the substrates were pre-wetted with deionized water, and the PEDOT:PSS solution of 50 μL was dropped onto the rotating substrates right after starting the spin-coating at 5000 rpm for 30 s. The MAPbI₃ perovskite layers were fabricated via Lewis base adduct method described by Ahn *et al.* A 1:1:1 molar ratio mixture of PbI₂ (Alfa Aesar), MAI (in-house synthesized), and dimethyl sulfoxide (DMSO) (Sigma-Aldrich) was dissolved in dimethylformamide (DMF) at 50 wt% without heating. The fully dissolved solution was spin coated onto the PEDOT:PSS layer at 3500 rpm for 20 s, with a dropping of 0.3 mL diethyl ether 8 s after starting the spin-coating process. The transparent green film, so-called CH₃NH₃I•PbI₂•DMSO adduct film, changed to a dark brownish color by heating at 65 °C for 1

min and 100 °C for 4 min. After that, the C₆₀ (20 nm), bathocuproine (BCP) (10 nm), LiF (0.5 nm), and Al (150 nm) were thermally deposited on the substrates inside the vacuum thermal evaporator under 10⁻⁶ Torr. All the spin-coating processes were carried out in ambient condition.

Characterizations. SEM images were obtained using field-emission scanning electron microscopy (AURIGA, Zeiss) and the cross-sectional images were obtained using the same equipment from the samples milled by focused ion beam. Solar simulated AM 1.5G sunlight was generated with Oriel Sol3A solar simulator calibrated to give 100 mW cm² using a standard Si photovoltaic cell (RC-1000-TC-KG5-N, VLSI Standards). *J*-*V* curves were recorded with a Keithley 2400 source meter. The forward and reverse scan rate was set to 200 ms per 20 mV. The active area of the devices is 1.77 mm². External quantum efficiency (EQE) spectra were measured with a Newport IQE200 system equipped with a 300 mW Xenon light source and a lock-in amplifier. Sheet resistance was measured using a four-point probe (CMT-SERIES, Advanced Instrument Technology). Transmittance was measured by UV-vis spectroscopy (Cary 5000, Agilent). Atomic force microscopy (AFM; Multi-mode, Bruker) topography images were recorded in tapping mode. Silicon AFM probes, with a nominal frequency of 70 kHz was used. Fermi levels were measured by RikenRiken Keiki PYS-A AC-2 in air. Both homemade systems based on Seki Technotron STR-250 (excitation wavelength 532 nm) and inVia Raman microscope (Renishaw) were used for the Raman measurement.

ASSOCIATED CONTENT

Supporting Information

AUTHOR INFORMATION

Corresponding Authors

mchoi@snu.ac.kr

maruyama@photon.t.u-tokyo.ac.jp

matsuo@photon.t.u-tokyo.ac.jp

ACKNOWLEDGEMENTS

I.J. thanks the Research and Education Consortium for Innovation of Advanced Integrated Science by Japan Science and Technology (JST) for financial support. This work was supported by JSPS KAKENHI (JP25107002, JP15H05760, JP16K05948, and JP16H06333) and IRENA Project by JST-EC DG RTD, Strategic International Collaborative Research Program, SICORP. Part of this work is based on results obtained from a project commissioned by the New Energy and Industrial Technology Development Organization (NEDO). This work was partly supported by the MOPPI project of the Aalto University AEF research program. + These authors contributed equally.

REFERENCES

- (1) Zhou, H.; Chen, Q.; Li, G.; Luo, S.; Song, T. -b.; Duan, H.-S.; Hong, Z.; You, J.; Liu, Y.; Yang, Y. *Science* **2014**, 345, 542–546.
- (2) Jeon, N. J.; Noh, J. H.; Yang, W. S.; Kim, Y. C.; Ryu, S.; Seo, J.; Seok, S. Il. *Nature* **2015**, 517, 476–480.
- (3) Grätzel, M. *Nat. Mater.* **2014**, 13, 838–842.
- (4) Green, M. A.; Ho-Baillie, A.; Snaith, H. J. *Nat. Photonics* **2014**, 8, 506–514.
- (5) Im, J.-H.; Jang, I.-H.; Pellet, N.; Grätzel, M.; Park, N.-G. *Nat. Nanotechnol.* **2014**, 9, 927–932.
- (6) Kim, H.; Lim K.-G.; Lee T.-W. *Energy Environ. Sci.*, **2016**, 9, 12-30.
- (7) Li, X.; Bi, D.; Yi, C.; Decoppet, J.-D.; Luo, J.; Zakeeruddin, S. M.; Hagfeldt, A.; Gratzel, M. *Science* **2016**, 353, 58–62.
- (8) Seo, J.; Noh, J. H.; Seok, S. Il. *Acc. Chem. Res.* **2016**, 49, 562–572.
- (9) Gomez De Arco, L.; Zhang, Y.; Schlenker, C. W.; Ryu, K.; Thompson, M. E.; Zhou, C. *ACS Nano* **2010**, 4, 2865–2873.
- (10) Yeo, J.-S.; Kang, R.; Lee, S.; Jeon, Y.-J.; Myoung, N.; Lee, C.-L.; Kim, D.-Y.; Yun, J.-M.; Seo, Y.-H.; Kim, S.-S.; Na, S.-I. *Nano Energy* **2015**, 12, 96–104.
- (11) Jeon, I.; Chiba, T.; Delacou, C.; Guo, Y.; Kaskela, A.; Reynaud, O.; Kauppinen, E. I.; Maruyama, S.; Matsuo, Y. *Nano Lett.* **2015**, 15, 6665–6671.
- (12) You, P.; Liu, Z.; Tai, Q.; Liu, S.; Yan, F. *Adv. Mater.* **2015**, 27, 3632–3638.
- (13) Iijima, S.; Ichihashi, T. *Nature* **1993**, 363, 603–605.

- (14) Du, J.; Pei, S.; Ma, L.; Cheng, H.-M. *Adv. Mater.* **2014**, *26*, 1958–1991.
- (15) Maiti, U. N.; Lee, W. J.; Lee, J. M.; Oh, Y.; Kim, J. E. J. Y.; Kim, J. E. J. Y.; Shim, J.; Han, T. H.; Kim, S. O. *Adv. Mater.* **2014**, *26*, 40–67.
- (16) Sun, D.-M.; Liu, C.; Ren, W.-C.; Cheng, H.-M. *Small* **2013**, *9*, 1188–1205.
- (17) Yang, F.; Wang, X.; Zhang, D.; Yang, J.; Luo, D.; Xu, Z.; Wei, J.; Wang, J.-Q.; Xu, Z.; Peng, F.; Li, X.; Li, R.; Li, Y.; Li, M.; Bai, X.; Ding, F.; Li, Y. *Nature* **2014**, *510*, 522–524.
- (18) Hatton, R. A.; Miller, A. J.; Silva, S. R. P. *J. Mater. Chem.* **2008**, *18*, 1183.
- (19) Nasibulin, A. G.; Kaskela, A.; Mustonen, K.; Anisimov, A. S.; Ruiz, V.; Kivistö, S.; Rackauskas, S.; Timmermans, M. Y.; Pudas, M.; Aitchison, B.; Kauppinen, M.; Brown, D. P.; Okhotnikov, O. G.; Kauppinen, E. I. *ACS Nano* **2011**, *5*, 3214–3221.
- (20) Kaskela, A.; Nasibulin, A. G.; Timmermans, M. Y.; Aitchison, B.; Papadimitratos, A.; Tian, Y.; Zhu, Z.; Jiang, H.; Brown, D. P.; Zakhidov, A.; Kauppinen, E. I. *Nano Lett.* **2010**, *10*, 4349–4355.
- (21) Jeon, I.; Cui, K.; Chiba, T.; Anisimov, A.; Nasibulin, A. G.; Kauppinen, E. I.; Maruyama, S.; Matsuo, Y. *J. Am. Chem. Soc.* **2015**, *137*, 7982–7985.
- (22) Li, Z.; Kulkarni, S. A.; Boix, P. P.; Shi, E.; Cao, A.; Fu, K.; Batabyal, S. K.; Zhang, J.; Xiong, Q.; Wong, L. H.; Mathews, N.; Mhaisalkar, S. G. *ACS Nano* **2014**, *8*, 6797–6804.
- (23) Aitola, K.; Sveinbjörnsson, K.; Correa-Baena, J.-P.; Kaskela, A.; Abate, A.; Tian, Y.; Johansson, E. M. J.; Grätzel, M.; Kauppinen, E. I.; Hagfeldt, A.; Boschloo, G. *Energy Environ. Sci.* **2016**, *9*, 461–466.
- (24) Cui, K.; Anisimov, A. S.; Chiba, T.; Fujii, S.; Kataura, H.; Nasibulin, A. G.; Chiashi, S.; Kauppinen, E. I.; Maruyama, S.; Online, V. A.; Cui, K.; Anisimov, A. S.; Chiba, T.; Fujii, S.; Kataura, H.; Nasibulin, A. G.; Chiashi, S.; Kauppinen, E. I.; Maruyama, S. *J. Mater. Chem. A* **2014**, *2*, 11311–11318.
- (25) Novoselov, K. S. *Science* **2004**, *306*, 666–669.
- (26) Song, Y.; Li, X.; Mackin, C.; Zhang, X.; Fang, W.; Palacios, T.; Zhu, H.; Kong, J. *Nano Lett.* **2015**, *15*, 2104–2110.
- (27) Shi, E.; Li, H.; Yang, L.; Zhang, L.; Li, Z.; Li, P.; Shang, Y.; Wu, S.; Li, X.; Wei, J.; Wang, K.; Zhu, H.; Wu, D.; Fang, Y.; Cao, A. *Nano Lett.* **2013**, *13*, 1776–1778.
- (28) Lee, Y.; Tu, K.-H.; Yu, C.; Li, S.; Hwang, J.-Y.; Lin, C.; Chen, K.-H.; Chen, L.-C.; Chen, H.-L.; Chen, C.-W. *ACS Nano* **2011**, *5*, 6564–6570.
- (29) Park, H.; Kong, J. *Adv. Energy Mater.* **2014**, *4*, 1301280.
- (30) Sung, H.; Ahn, N.; Jang, M. S.; Lee, J.; Yoon, H.; Park, N.; Choi, M. *Adv. Energy Mater.* **2016**, *6*, 1501873.
- (31) Kim, H.; Byun, J.; Bae, S.-H.; Ahmed, T.; Zhu, J.-X.; Kwon, S.-J.; Lee, Y.; Min, S.-Y.; Wolf, C.; Seo, H.-K.; Ahn, J.-H.; Lee, T.-W. *Adv. Energy Mater.* **2016**, *6*, 1600172.
- (32) Hellstrom, S. L.; Vosgueritchian, M.; Stoltenberg, R. M.; Irfan, I.; Hammock, M.; Wang,

- Y. B.; Jia, C.; Guo, X.; Gao, Y.; Bao, Z. *Nano Lett.* **2012**, *12*, 3574–3580.
- (33) Han, T.-H.; Lee, Y.; Choi, M.-R.; Woo, S.-H.; Bae, S.-H.; Hong, B. H.; Ahn J.-H.; Lee T.-W. *Nat. Photon.* **2012**, *6*, 105–110.
- (34) Jeon, I.; Delacou, C.; Kaskela, A.; Kauppinen, E. I.; Maruyama, S.; Matsuo, Y. *Sci. Rep.* **2016**, *6*, 31348.
- (35) Kuruvila, A.; Kidambi, P. R.; Kling, J.; Wagner, J. B.; Robertson, J.; Hofmann, S.; Meyer, J. *Mater. Chem. C* **2014**, *2*, 6940–6945.
- (36) Di Giacomo, F.; Fakharuddin, A.; Jose, R.; Brown, T. M. *Energy Environ. Sci.* **2016**, *9*, 3007–3035.
- (37) Yoon, J.; Sung, H.; Lee, G.; Cho, W.; Ahn, N.; Jung, H. S.; Choi, M. *Energy Environ. Sci.* **2017**, *10*, 337–345.
- (38) Ahn, N.; Son, D.-Y.; Jang, I.-H.; Kang, S. M.; Choi, M.; Park, N. *J. Am. Chem. Soc.* **2015**, *137*, 8696–8699.
- (39) Liu, P.; Liu, X.; Lyu, L.; Xie, H.; Zhang, H.; Niu, D.; Huang, H.; Bi, C.; Xiao, Z.; Huang, J.; Gao, Y. *Appl. Phys. Lett.* **2015**, *106*, 193903.
- (40) Park, H.; Brown, P. R.; Bulović, V.; Kong, J. *Nano Lett.* **2012**, *12*, 133–140.
- (41) Jeon, I.; Qian, Y.; Nakao, S.; Ogawa, D.; Xiang, R.; Inoue, T.; Chiashi, S.; Hasegawa, T.; Maruyama, S.; Matsuo, Y. *J. Mater. Chem. A* **2016**, *4*, 18763–18768.
- (42) Bissett, M. A.; Izumida, W.; Saito, R.; Ago, H. *ACS Nano* **2012**, *6*, 10229–10238.
- (43) Lee, C.; Wei, X.; Kysar, J. W.; Hone, J. *Science* **2008**, *321*, 385–388.
- (44) Guinea, F.; Katsnelson, M. I.; Geim, A. K. *Nat. Phys.* **2010**, *6*, 30–33.
- (45) Yeh, N. C.; Teague, M. L.; Yeom, S.; Standley, B. L.; Wu, R. T. P.; Boyd, D. A.; Bockrath, M. W. *Surf. Sci.* **2011**, *605*, 1649–1656.
- (46) Huang, M.; Yan, H.; Heinz, T. F.; Hone, J. *Nano Lett.* **2010**, *10*, 4074–4079.
- (47) Kotakoski, J.; Meyer, J. C. *Phys. Rev. B* **2012**, *85*, 195447.
- (48) Hao, F.; Fang, D. *Phys. Lett. A* **2012**, *376*, 1942–1947.
- (49) Grantab, R.; Shenoy, V. B.; Ruoff, R. S. *Science* **2010**, *330*, 946–948.
- (50) Duong, D. L.; Han, G. H.; Lee, S. M.; Gunes, F.; Kim, E. S.; Kim, S. T.; Kim, H.; Ta, Q. H.; So, K. P.; Yoon, S. J.; Chae, S. J.; Jo, Y. W.; Park, M. H.; Chae, S. H.; Lim, S. C.; Choi, J. Y.; Lee, Y. H. *Nature* **2012**, *490*, 235–239.
- (51) Yu, Q.; Jauregui, L. A.; Wu, W.; Colby, R.; Tian, J.; Su, Z.; Cao, H.; Liu, Z.; Pandey, D.; Wei, D.; Chung, T. F.; Peng, P.; Guisinger, N. P.; Stach, E. A.; Bao, J.; Pei, S.-S.; Chen, Y. P. *Nat. Mater.* **2011**, *10*, 443–449.
- (52) Wang, S.; Suzuki, S.; Hibino, H. *Nanoscale* **2014**, *6*, 13838–13844.
- (53) Ferrari, A. C.; Robertson, J. *Phys. Rev. B* **2000**, *61*, 14095–14107.

- (54) Mohiuddin, T. M. G.; Lombardo, A.; Nair, R. R.; Bonetti, A.; Savini, G.; Jalil, R.; Bonini, N.; Basko, D. M.; Galiotis, C.; Marzari, N.; Novoselov, K. S.; Geim, A. K.; Ferrari, A. C. *Phys. Rev. B* **2009**, 79, 205433.
- (55) Malard, L. M.; Pimenta, M. A.; Dresselhaus, G.; Dresselhaus, M. S. *Phys. Rep.* **2009**, 473, 51–87.
- (56) Tuan Hung, N.; Van Truong, D.; Van Thanh, V.; Saito, R. *Comput. Mater. Sci.* **2016**, 114, 167–171.
- (57) Sakhaee-Pour, A. *Solid State Commun.* **2009**, 149, 91–95.
- (58) Li, Y.; Meng, L.; Yang, Y.; Xu, G.; Hong, Z.; Chen, Q.; You, J.; Li, G.; Yang, Y.; Li, Y. *Nat. Commun.* **2016**, 10214